Microphysical properties of cold frontal rainbands

J. Crosier[1,2], T. W. Choularton[2], C. D. Westbrook[3], A. M. Blyth[4,5], K. N. Bower[2], P. J. Connolly[2], C. Dearden[2], M. W. Gallagher[2] , Z. Cui[5], J. C. Nicol[6,3]

[1]National Centre for Atmospheric Science, University of Manchester, UK

[2]Centre for Atmospheric Science, University of Manchester, UK

[3]Department of Meteorology, University of Reading, UK

[4]National Centre for Atmospheric Science, University of Leeds, UK

[5]School of Earth and Environment, University of Leeds, UK

[6]National Centre for Atmospheric Science, University of Reading, UK

Keywords: Ice multiplication, Cold front, Rainband, In-situ, Radar, Precipitation

Abstract

Observations have been obtained within an intense (precipitation rates > 50 mm hour^{-1}) narrow cold-frontal rainband (NCFR) embedded within a broader region of stratiform precipitation. In-situ data were obtained from an aircraft which flew near a steerable dual-polarisation Doppler radar. The observations were obtained to characterise the microphysical properties of cold frontal clouds, with an emphasis on ice and precipitation formation and development.

Primary ice nucleation near cloud top (-55°C) appeared to be enhanced by convective features. However, ice multiplication led to the largest ice particle number concentrations being observed at relatively high temperatures (> -10°C). The multiplication process (most likely rime-splintering) occurs when stratiform precipitation interacts with supercooled water generated in the NCFR. Graupel was notably absent in the data obtained.

Ice multiplication processes are known to have a strong impact in glaciating isolated convective clouds, but have rarely been studied within larger organised convective systems such as NCFRs. Secondary ice particles will impact on precipitation formation and cloud dynamics due to their relatively small size and high number density. Further modelling studies are required to quantify the effects of rime splintering on precipitation and dynamics in frontal rainbands. Available parameterizations used to diagnose the particle size distributions do not account for the influence of ice multiplication. This deficiency in parameterizations is likely to be important in some cases for modelling the evolution of cloud systems and the precipitation formation. Ice multiplication has significant impact on artefact removal from in-situ particle imaging probes.

1. Introduction

Mature mid-latitude cyclones often have one or more distinct precipitation features associated with them. The location of the features with respect to the moving frontal system, as well as the intensity of precipitation, is indicative of the processes that form them. A summary of the precipitation features (referred to as rainbands, due to their banded structure) associated with mid-latitude cyclones can be found in Matejka et al (1980). Matejka et al (1980) introduced the concept of two types of rainband associated with cold frontal passage: Narrow and Wide Cold Frontal Rainbands (referred to as NCFR and WCFR respectively).

The NCFR is a region of heavy precipitation typically orientated along the surface cold front. Precipitation in the NCFR is formed due to intense line convection generated near the surface, where rearward sloping cold air undercuts and lifts the moist warm sector air approaching the surface cold front, in a system-relative sense (Browning 1986). NCFR's can be over 100 km in length along the surface cold front, but are only a few km in width, and can generate precipitation rates as high as 100 mm hr^{-1}. These high precipitation rates are observed at the surface for only a few minutes as the system passes overhead. Passage of a NCFR also results in sudden drops in temperature/wind speed, a veer in the wind direction, and a jump in pressure at the surface (James and Browning 1979). Browning and Reynolds (1994) highlight an additional mechanism for NCFR generation, via the downward transport of stratospheric air, leading to strong surface gusts which initiate convection.

The line of intense precipitation associated with a NCFR is frequently broken into smaller elements (referred to as precipitation cores) separated by a quiescent region of suppressed precipitation called a gap region (James and Browning 1979, Hobbs and Persson 1982, Browning and Roberts 1996). The smaller bands of heavy precipitation range in size from a few km to tens of km in length, while still remaining a few km wide. The gap regions can be of a similar size to the precipitation cores, but are typically smaller (Locatelli et al 1995). Locatelli et al (1995) and Jorgensen et al (2003) discuss the positive feedback between convection and precipitation: the effect of cooling in the cold sector by evaporation/melting of precipitation leads to enhanced baraclinicity, and strengthens cold-air advection and thus convection.

The WCFR is a region of light precipitation which spans the front over a greater horizontal extent (several tens of km), along the length of the surface cold front (Matejka et al 1980). It results from the gradual slantwise ascent at mid/upper levels which occurs during frontal passage. The position of the NCFR with respect to the WCFR, and the formation of gap regions in the NCFR are largely determined by the position of the upper level cold front relative to the surface cold front (Browning 1986, Browning and Roberts 1996). This is itself determined by the progression of the dry intrusion around the trough and into the cloudy warm conveyor belt region.

The CYCLES PROJECT (Matejka et al 1980) and IMPROVE (Stoelinga et al 2001) field campaigns examined the roles of dynamics and microphysics in rainbands associated with frontal systems through a combination of airborne in-situ microphysics, Doppler radar, radiosondes and surface observations. For example, Rutledge and Hobbs (1984) concluded that efficient graupel production (facilitated by liquid water generation due to rapid ascent at the surface cold front) was responsible for the majority of the precipitation in the NCFR. They also observed high ice particle number concentrations in this same region (attributed to rime splintering, Hallett and Mossop 1974), but these ice particles did not contribute significantly to the precipitation.

As has just been discussed, the precipitation and dynamical structure of NCFRs has been investigated by several studies over the past three decades. However, there have been relatively few studies which have examined the cloud microphysical properties of such systems in detail. Those which have are likely affected by artefacts which were unknown/uncorrected at the time. In this paper we present airborne in-situ microphysics, surface observations and dual polarisation Doppler radar measurements from cloud associated with a cold front that has a NCFR embedded within a WCFR. The measurements presented are obtained using the most up-to-date probes at the time, and processed to eliminate potential artefacts which have only recently been identified (Field et al 2006, Korolev et al 2011). Our results are compared qualitatively with those from the previous studies which may have been affected by these artefacts.

2. Methodology

Measurements of cloud microphysical properties were collected in mixed phase clouds in the UK during 2007-2010 as part of the NERC-funded Aerosol Properties, PRocesses And InfluenceS on the Earth's climate (APPRAISE) programme, Clouds project (APPRAISE-Clouds). In-situ measurements were collected on-board the UK Facility for Airborne Atmospheric Measurement (FAAM) BAe-146 aircraft. Remote sensing measurements were also performed at the Chilbolton Facility for Atmospheric and Radio Research (CFARR) in southern England (51.14° N, 1.44° W). Objectives of APPRAISE-Clouds focus on the impact of aerosols on cloud micro-physical properties (Crosier et al 2011; Westbrook and Illingworth, 2011; Crawford et al 2012; Cui et al 2012). We present measurements collected on 3 March 2009, in cloud associated with a cold frontal system which passed over CFARR at approximately 2035 UTC. A summary of the instrumentation used can be found below. Additional information on instrumentation can be found in Crosier et al (2011).

In-situ microphysical measurements onboard the BAe-146 were obtained from a CDP (Lance et al 2010), CIP-15, CIP-100 (Baumgardner et al 2001) and 2D-S (Lawson et al 2006). Particle Inter-Arrival Time (IAT) filtering was applied to remove shattering artefacts (Field et al 2006) from the CIP-15 and CIP-100 data. Details of the IAT thresholds used are described later in the paper. Anti-shatter tips to prevent sampling artefacts (as described by Korolev et al 2011) were not fitted for this study. The CIP-15 and CIP-100 data were also merged to create a synthesised size distribution from ~60-6200 µm. The change over between the 15 and 100 micron resolution probe occurred at ~550 µm and was decided upon by considering both sample volume and image resolution. Particle size (D_p) is defined as the average of the maximum size in the along (D_y) and across (D_x) array directions. Note this differs from the commonly used D_x size, which is sensitive to orientation for elongated particles. The sizing metric we use exhibits weaker sensitivity (approximately by a factor of two) to particle orientation, which is important when trying to capture the true size distribution in areas dominated by elongated particles such as those which we highlight in this paper. We have used the "all-in" sample volume approach (Heymsfield and Parish, 1978) and so reject partially imaged particles. The 2D-S is used in this paper to provide higher resolution (10 μm pixel) images of the measured particles. It was not used in the size distributions as it suffered from technical problems at high altitude (T < -38°C). In-situ observations of vertical air motions were not obtained due to the 5-hole turbulence probe (mounted on the aircraft nose radome) experiencing technical problems in the icing conditions.

Remote sensing of precipitation-sized particles was performed using the Chilbolton Advanced Meteorological Radar, (CAMRa, Goddard et al, 1994), a steerable 3 GHz dual-polarisation Doppler radar with a narrow 0.28° beam. The BAe-146 aircraft was only able to operate along the 255° radial (WSW) because of air-traffic control restrictions therefore RHI (range height indicator) scans were made by CAMRa continuously along this radial.

Vertical air motion may be estimated using Doppler velocity measurements from RHIs by assuming mass-weighted flow continuity (e.g. Chapman and Browning 1998). At low elevation angles (less than about 10°), the Doppler velocity is approximately equal to the radial component of the horizontal wind as the influence of vertical air motion and the vertical fall speeds of the targets (e.g. rain) may be neglected. Vertical air velocities (w) may then be estimated by integrating the observed convergence of the radial wind throughout each column assuming the boundary condition w=0 at some height and taking density changes with height into account. We have chosen to integrate downwards, assuming that w=0 at the echo top, as the radar is unable to sample sufficiently close to the surface except at very close ranges. Errors related to this assumption will exist throughout each column, however it is likely that vertical motions at the echo top will be significantly weaker than in the updraught near the surface at the frontal boundary and can largely be neglected. This technique also requires that there is negligible divergence into the plane of the RHI; based on the linear structure of the NCFR, we shall assume that this is true.

3. Results and Discussion

A cold frontal system passed over the UK on 3 March 2009, arriving at the western coast at ~1800 UTC. Widespread precipitation was associated with the passage of this front, in the form of a WCFR with low/moderate intensity of precipitation (P < 10 mm hr^{-1}). A NCFR of much higher precipitation intensity (P > 50 mm hr^{-1}) was also present and (as is characteristic of such rainbands) only affected a narrow region along the surface cold front. In the following paragraphs the synoptic situation and the rainband structure will be described. We then shift emphasis on to the microphysics of the rainband.

3.1 Synoptic Overview

Figure 1 presents an overview of the synoptic situation at 1800 UTC using ECMWF operational analysis data (0.25° resolution). Data shown in Figure 1a are mean sea level pressure contours and equivalent potential temperature at 500 hPa. The location of the CFARR ground site is marked as a black cross. A trough located between the UK and Iceland was associated with the advection of cold air to the southeast, where it intercepted a tongue of warmer air. The warmer air flowed to the north at the eastern side of the trough in the form of a warm conveyor belt (Browning 1986). Kinks in the sea-level isobars over Ireland/Celtic Sea (coincident with the region of rapidly changing equivalent potential temperature, θ_e), indicate the presence of a cold front.

Vertical cross sections (along 51.24° latitude) of θ_e and relative humidity fields are shown in Figures 1b and 1c, respectively. The θ_e cross section (Fig. 1b) highlights the cold sector found to the west of the trough (CS1) and the warm sector (WS) adjacent to this on the eastern side of the front. The boundary between these represents the cold frontal surface

(Browning 1986). To the east of the warm sector, another cold sector (CS2) is visible. The transition between the WS and CS2 represents the warm front associated with the cyclone. This is not the focus of this paper but is mentioned to identify all the features found within the figure. The relative humidity field (Fig. 1c) shows a region of dry air above CS1. This suggests that overrunning of the cloudy warm conveyor air by the dry intrusion has occurred at this location, which fits the description of a kata-type cold front (Browning and Roberts 1996). However, the rearward-sloping ascent/line convection observed is an ana-type characteristic (Agusti-Panareda et al, 2009), so this case is some form of hybrid of the two types. The WS is characterized by high relative humidity due to the mesoscale ascent.

The corresponding Infrared satellite image (1800 UTC from MSG) is shown in Figure 2. A large continuous band of cloud associated with ascent in the warm conveyor belt is located over the Celtic Sea, Bay of Biscay and mainland UK. Cloud top temperatures in the warm sector frontal clouds were of the order of -50°C according to both the ECMWF analysis data and from the multi-channel MSG retrieval (albeit with significant variations of approx +/- 10°C using the latter). To the northwest of this frontal cloud, the cold sector has a more broken cloud field, some parts of which have significantly warmer cloud top temperatures (around -10°C). There is possible evidence for the erosion of upper level clouds by the dry intrusion occurring over the Irish Sea.

3.2 Rainband structure

The precipitation structure for the frontal system of interest is shown in Figure 3 using data from the UK Met Office operational radar network (NIMROD). Data are shown for three times, 1800, 1900 and 2000 UTC to show the temporal evolution. Figures 3(a-c) show a region of moderate precipitation (1-10 mm hr^{-1}) which follows the approximate location of the cold front as inferred from the infrared satellite image (Figure 2) and ECMWF analysis (Figure 1). This precipitation band is typically 100 km wide, and is either a WCFR or a warm sector rainband (but most likely a combination of the two). Regions of high precipitation rate are also observed but are not easily visible due to their small size.

Figures 3 (d-f) show precipitation rates in the vicinity of the CFARR ground site.. A narrow band of heavy precipitation only a few km wide can be seen to the west of CFARR at 1800 UTC (Figure 3d), which moves to the east with time. The detailed structure of the narrow rainband alters as it moves to the east, with some evidence of kinks and gaps at some times and not others. However, the general structure of the rainband (southwest to northeast orientation, precipitation rates, $P > 20$ mm hr^{-1}) changes little. This narrow band of heavy precipitation is the NCFR mentioned in previous studies. The NCFR passed over the CFARR ground site (indicated on Figures 3(d-f) by a red circle) at ~2035 UTC.

Surface observations from CFARR are shown in Figure 4. The passage of the rainband occurs at ~2035 UTC, with precipitation rates greater than 60 mm hr^{-1} observed for about one minute using a rapid-response drop-counting raingauge (Norbury and White 1971). Rapid changes in temperature ($-3^{\circ}C$), wind speed and direction were also observed at approximately the same time. This corresponds with the switch in airmass at the surface from the (relatively) meridional warm sector to the (relatively) zonal cold sector (Figure 4a). A characteristic positive jump in the (generally descending) pressure is also seen. Precipitation rates either side of the narrow rainband (in the WCFR) were of the order 1-10 mm hr^{-1}. Upon close inspection, it becomes apparent that the NCFR was observed before the changes in wind speed/direction, and the drop in temperature.

3.3 Rainband Microphysics – Remote Sensing

Example RHI scans of radar reflectivity factor (dBZ_h, from the horizontal polarisation) and unfolded Doppler velocity (v_u) from CAMRa are shown in Figures 5 and 6. Reported Doppler velocities are positive for motions towards the radar. The scans shown were conducted between 19:22:07 - 19:23:07 and 20:03:00 – 20:04:00 for Figures 5 and 6 respectively. Both RHIs were obtained along the 255° radial, whilst the BAe-146 aircraft was sampling in-situ along the same radial. The scan was conducted to the southwest, so the x-axis has been reversed to aid visual interpretation. The detection limit of dBZ_h is -20 at 10 km range, which rises to $dBZ_h = 0$ at 100 km range.

The general features, as shown in Figures 5a and 6a, are low values of reflectivity near cloud top ($dBZ_h < 0$), a bright band ($dBZ_h > 30$) near the melting layer (1-2 km altitude) and typical dBZ_h values of 15-30 at mid-levels. Fallstreaks are present near cloud top (especially in Figure 6a), which suggests convective cells are generating ice particles. Cloud top (according to radar reflectivity) varies between 5-8 km. Some of the variability in cloud top is a result of the variable detection limit with range, but also due to the fallstreak structure observed. Figure 5a shows a bump in the bright band at approximately 57-60 km from CFARR, where the high values of dBZ_h were observed at higher altitudes (up to 2 km) than the surrounding regions. This enhancement in dBZ_h is located above the surface cold front (see below), and indicates the location of the NCFR. This reflectivity feature marking the NCFR is located ~25km from CFARR according to the RHI obtained 40 minutes later (as shown in Figure 6a). Vertical profiles of dBZ_h, extracted from the RHI scan in Figure 5a, are shown in Figure 7e. The profiles are taken from a distance -10, 0, 10 and 20 km from the centre of the NCFR (positive values being closer to CFARR, downwind of the cold front), and show the impact of both the brightband and NCFR on the dBZ_h structure at lower/mid levels. The dBZ_h structure at upper levels is nearly identical between profiles.

Figure 5b shows a large rearward sloping region of relatively slow moving targets ($v_u < 35$ ms^{-1}). This large feature represents the location of the boundary between warm and cold air (i.e. slantwise ascent at the cold frontal boundary). The rear-inflow jet which drives the advection/convection is identified by the region of high Doppler velocity ($v_u > 35$ ms^{-1}), located beneath the slanted cold front boundary already mentioned. The smallest values of v_u found in this feature are approx 60 km from CFARR, coincident with the region of elevated dBZ_h (Figure 5b) discussed previously.

Other large-scale features which can be seen in the velocity data (Figure 5b) include; the low-level jet (LLJ), a region of high wind and low turbulence (as indicated by low Doppler spectral width, not shown) ahead of the cold front (10-50 km distance, 1-4 km altitude), which flows along the length of the front (Jorgensen et al 2003); boundary layer convection ahead of the cold front (10-50 km distance, altitudes less than 1 km) as indicated by low Doppler velocities and increased turbulence. The velocities in this boundary layer are significantly lower than in the low level jet above due to friction at the surface.

The vertical velocity field estimated using the technique described in section 2 is shown in Figure 5d, indicating a near-vertical line of convection occurring at the surface cold front. The peak updraught velocity (6.9 ms^{-1}) occurs near the surface in association with the cold front and significant updraughts (at least 2 ms^{-1}) extend up to 2 km. Doppler velocities were averaged onto a 1 km (horizontal) by 250 m (vertical) Cartesian grid to derive the vertical wind speeds depicted in Figure 5d. Vertical velocity calculations made at a finer horizontal resolution (500 m) estimated a more intense updraught associated with the NCFR (peak updraught = 8.2 ms^{-1}). The updraughts in the NCFR below 2 km altitude at 500 m horizontal resolution were 30 percent larger on average than at 1 km resolution. Lesser differences were found at finer resolutions, approaching the range-resolution of the radar measurements (300 m).

Also shown in Figure 5 is the Differential Reflectivity (Z_{DR}, figs. 5c) from CAMRa. In the bulk of the stratiform cloud above the melting layer the differential reflectivity (Z_{DR} < 0.5 dB) is consistent with the presence of irregular aggregates and polycrystals (Wolde and Vali 2001). However, elevated values of Z_{DR} (1-2 dB) can be seen in two main areas of the RHI scans (figs. 5 c). First, they can be seen in/around cloud top, specifically in regions where fallstreaks are apparent. This suggests pristine ice particle formation in/around cloud top (Wolde and Vali 2001, Bailey and Hallett 2009), in convectively active regions. By pristine ice, we refer to ice particles which have not undergone either aggregation or riming, and so have grown by vapour deposition alone. Note that in these regions Z_{DR} is negatively correlated with dBZ_h. The regions of higher dBZ_h are likely composed of polycrystalline or aggregated ice particles with lower Z_{DR}. The fallstreak structure and anticorrelation between dBZ_h and Z_{DR} suggests that there is some 'sorting' mechanism, perhaps the result of different fall speeds of the two different crystal types. It is worth noting that the Z_{DR} structures could also result from partially rimed/aggregated/sublimated particles.

The second region where high Z_{DR} is observed is a layer at 3-4 km altitude (highlighted by the grey oval in Figure 5c), forming a wide inverted U shape, overlying the NCFR. This layer extends for around 30 km in the horizontal, and suggests that some kind of pristine ice particles exist (and are possibly forming) at this level. Subsequent and previous RHI scans show this layer advects towards CFARR with time, with the particles which constitute this layer slowly decending to the surface (at a rate of a few km per hour). Its position extends ahead of the leading edge of the surface cold front, due to wind shear in the vertical. Regions of high differential reflectivity (up to 3 dB) have been observed in regions of embedded convection within frontal cloud, and were associated with pristine columns formed by ice multiplication (Hogan et al 2002).

The observations presented in Figure 5 fit the conceptual model of a NCFR well (Locatelli et al 1995, Jorgensen et al 2003): narrow upright updraught ($w > 7$ m s^{-1}) coinciding with high reflectivities ($dBZ_h > 30$) above the melting layer, both of which are located above a surface cold front.

3.4 Rainband Microphysics – In-situ data

3.4.1 Bulk in-situ properties

A summary of the in-situ microphysical properties of the cloud associated with the cold front can be found in Figure 7. The merged CIP-15/100 data are put into 500 m altitude bins for the whole flight. This includes data from both the NCFR and WCFR. Parameters shown include total number concentration (N_{tot}), mean diameter (D_{mean}), and the second moment of the number concentration distribution (M2). We have shown M2 as it is approximately proportional to the mass concentration according to Locatelli and Hobbs (1974), Brown and Francis (1995) and Heymsfield et al (2007, 2010). These studies related particle mass to diameter using two parameters, a and b, using the form Mass = a x Diameter^b. The aforementioned studies have shown that b has a value ranging from 1.8 - 2.2). One limitation of using M2 to represent mass is that it does not take variations in density with particle type into account. Also shown in Figure 7 is the ambient temperature in each altitude bin.

Figure 7(a) shows that large values of particle number concentration are observed at -55°C, near cloud top (median N_{tot} ~60 L^{-1}, maximum N_{tot} > 100 L^{-1}). Note the median concentrations in the highest altitude bin (8.5-9.0 km) are smaller than in the bin below. This is probably due to the ice particles being too small for the imaging probes to detect. Also, cloud top may have varied somewhat during the pass. At lower altitudes, median N_{tot} is significantly lower than these cloud top concentrations, most likely due to the effects of aggregation and size sorting. An important exception is seen in the 2.0-2.5 km altitude bin (T = -8°C), where a second maximum is observed (median N_{tot} ~10 L^{-1}, maximum N_{tot} >100 L^{-1}). This coincides with the Hallett-Mossop (HM) zone (-3 to -8°C, Hallett and Mossop, 1974) and suggests that ice multiplication is occurring via rime-splinter ejection. Large maximum values of N_{tot} are enhanced in the surrounding altitude bins. This suggests that these secondary ice particles are being transported within the cloud. Images of the ice particles in this region show large numbers of pristine columns (100-400 µm length), which is the main growth habit at these relatively high temperatures. Secondary maxima in ice particle number concentration at approx. -8°C were also observed by Bower et al (1996) in frontal clouds over the UK.

The profile of D_{mean} is shown in Figure 7(b). The smallest particles are found at cloud top (D_p < 100 µm), with D_{mean} increasing to ~1 mm at 4 km altitude. This is largely consistent with the concept of snow formation via aggregation and depositional growth of ice crystals. Significant increases in the variability of D_{mean} (as indicated by the shaded regions) are found at altitudes below 4 km. This is due to the influence of the smaller pristine columns (produced by multiplication in the HM zone) on the size distribution which would otherwise be dominated by larger snow particles. The profile of M2 shows a general increase with decreasing altitude. An increase in the variability of M2 can also be seen in the HM zone. In-situ data shown in Figure 5e demonstrates that the region of elevated M2 is co-located with the region of elevated N_{tot}. Therefore, rime splintering may be contributing to the observed increase in M2 (and thus the mass concentration). It should be noted that there were no instruments onboard the aircraft capable of phase discrimination of particles with $D_p < 50$ μm. These could have had a significant effect on the N_{tot} and D_{mean} profiles in Figure 7.

In-situ data from a subset of the flight are shown in Figure 5(e) and (f). The aircraft position during the period shown (19:09:00 - 19:27:36) is indicated by the black line in Figure 5(a-d), and coincides with the radar scan (19:22:07 - 19:23:07). The aircraft track skims the top of the high reflectivity/Doppler feature identified earlier as the NCFR. In this region a clear increase in the number concentration is observed (from $N_{tot} < 10$ L^{-1} to $N_{tot} > 100$ L^{-1}), and pristine columns presumably generated by HM multiplication tend to dominate. A corresponding increase in M2 (proportional to mass concentration) is also clearly apparent. Therefore, the HM multiplication process appears to be highly active in the NCFR, at least in terms of affecting number concentrations. The increase in M2 is partly related to the large number of particles from HM multiplication, as will be discussed in section 3.4.2.

Comparisons of the measured radar reflectivity (from the CAMRa data, extracted along the aircraft flight track), with that calculated using the in-situ data, are shown in Figures 5f and 6d. We have used the method outlined by Hogan et al (2006) to perform the calculation of reflectivity from in-situ data, using the mass-diameter relationship of Brown and Francis (1995). The reflectivity data from measurement and calculation agree to within 5-7 dBZ and show similar peaks/troughs in the data. The discrepancies can be accounted for in deviations from the mass-diameter relationship used, due to the dependency of radar reflectivity the square of the mass. A comparison of the measured and calculated Radar Reflectivity for the entire flight is shown in Figure 7f. When ignoring the reflectivity values which are enhanced due to the brightband at 0°C, the data compare very well ($R^2 = 0.83$), albeit with deviations from a 1:1 correlation (slope = 0.73).

During the aircraft pass shown in Figure 5, only minimal amounts of liquid water were detected (< 0.1 g m^{-3}). This may seem low considering the convective activity, but the aircraft passed over (and not within) the main reflectivity/convective feature. Therefore, updraughts in the region sampled may have been significantly lower than those in the updraught core. This could explain the depletion of liquid water, as the Wegener-Bergeron-Findeisen process would be active in the region sampled, because of the reduced availability of water vapour in the updraught and the presence of a large number of newly formed ice particles. No measurements of vertical wind speed are available from the BAe-146 due to instrument icing problems at this time. CFARR data (discussed earlier) suggests peak updraughts were less than 0.5 m s^{-1} during the pass by the aircraft. Based on the framework outlined by Korolev and Mazin (2003), the estimated minimum vertical velocity required to maintain supercooled cloud droplets given the measured ice particle population is of order 1 m s^{-1}. There are no passes through the region of greatest reflectivity within the NCFR by the BAe-146.

In-situ data obtained from a subsequent run at altitudes of 7 – 9 km are shown in Figure 6(c-d). Large regions of this RHI scan show no detectable radar return despite in-situ data confirming the presence of cloud ice particles in the same region. However, the calculated reflectivity from these regions is below the detection limit of the CAMRa. The RHI scan (Figure 6a) shows several isolated features protruding from the otherwise uniform cloud top. Ice particle number and mass (M2) concentrations are found to be much higher in this region. This suggests some form of convective activity enhancing nucleation when compared to the rather stable surrounding regions.

3.4.2 Particle size distributions

The changes of the particle size distribution with altitude are shown in Figure 8. These spectra (approx. five minute averages) are taken from periods where the BAe-146 was flying at constant altitude along the 255° radial. Also shown on Figure 8 are Cumulative Distribution Frequency (CDF) curves for the number concentration and second moment (M2), to provide an indication of which parts of the size distribution contribute to the total number concentration and M2 (or mass) respectively. These CDF curves are generated from the merged CIP-15/100 particle size distributions, and do not include the smallest particles ($D_p < 60$ µm) in order to exclude cloud droplets from the analysis. This conforms to the recommendations of Korolev (2007), that states images obtained with OAP probes which are less than 3-4 pixels wide should be ignored due to the digitization/depth of field uncertainties.

The spectra from near cloud top (e.g. Figure 8a-b) are narrow and unimodal. Images show these particles are pristine bullet-rosette type ice crystals. Lower down in the cloud (Figure 8c-e) a second mode forms at larger sizes ($D_p > 300$ µm), similar to that observed by Field (2000). These particles are more complex and aggregation appears to be important in forming these snow particles. The size distributions shown in Figures 8(e) and (f) are obtained at the same altitude/temperature, but are from outside and inside the region of high ice crystal concentration observed near the NCFR respectively. The spectrum obtained near the NCFR shows the large increase in particle number at smaller sizes (D_p < 1 mm), which are the HM secondary particles. Inspection of the imagery data reveals these small particles are dominated by ice particles, specifically columns.

The CDF curves in Figures 8f show that the contribution of particles with D_p < 400 μm is approximately 15% and 90% for M2 and number concentration respectively. The corresponding values for Figure 8e, (which was at the same altitude/temperature, but further away from the NCFR), are <10% and 3% for number concentration and M2 respectively. This shows a significant increase in the relative contribution to M2 (and thus mass) of the < 400 μm particles (which are mostly a result of the HM multiplication) in the NCFR.

A number of other studies in mid-latitude stratiform precipitation have derived parameterizations to fit the particle size distributions observed over many case studies. We have included these data in Figure 8, based on the parameterizations of Field et al 2005, Field et al 2007, and Woods et al 2008 (referred to as F05, F07 and W08 respectively). The F05 and F07 studies used identical approaches, invoking a "universal size distribution" that is scaled according to the second and third moments of the size distribution. The second moment is an input, and the third moment is predicted using a temperature-dependant parameterization. The universal size distribution contains three unique parameters which define its shape, and allows the representation of relatively complex size distributions. The W08 study used a temperature dependant parameterization to derive a two parameter negative exponential size distribution.

The agreement between the measured and parameterized size distributions is generally good for $D_p > 1000$ µm. Exceptions to this include Figure 8a (-56°C), where the comparison is not valid due to the lack of large particles, and Figure 8f(-10°C in the NCFR region), where W08 underestimates the large particle concentration by an order of magnitude. Below 1000 µm, most of the parameterizations over predict the number concentration by between one and two orders of magnitude. Exceptions to this can be seen in Figures 8b (-42°C) and 8f (-10°C in the NCFR region), where the agreement is within one order of magnitude. The quality of agreement between the measurements and parameterizations could be due to a number of reasons, including natural variability between cloud systems. However, what is clear is that the parameterizations available do not delineate between regions which are at the same temperature, but which are and are not influenced by the HM process. Therefore the accuracy of the parameterizations used to represent the PSD is likely to be compromised in (or near to) regions where the HM process is active (or in-active), such as the NCFR in this study. The level of over/under-prediction is dependent on the level of influence of the HM process on the dataset used to derive the parameterizations).

3.4.3 Particle Imagery

A summary of the particle habits observed at different altitudes/temperatures over all runs is shown in Figure 9. The images shown here are typical of those found at any given temperature. However, a large amount of variability is observed at any one time, especially when imaging small particles like bullet-rosettes near cloud top, and columns near the NCFR, and also aggregate particles.

Figure 9 reveals several interesting features. First of all, bullet rosette particles are detected near cloud top. This is the dominant growth regime at low (<-30°C) temperatures (Bailey and

Hallett 2009). The fallstreaks observed near cloud top (Figure 6a) suggest convection is driving nucleation by increasing the relative humidity and reducing cloud top temperatures (whilst increasing cloud top height). Also low cloud top temperatures (-55°C) lend weight to the idea of homogeneous nucleation being responsible for some of the observed ice formation. However, heterogenous nucleation can also be enhanced in such convective features, and we have no method to separate the action of each mechanism.

Secondly, low concentrations of relatively small (< 800 μm) pristine stellar plates and hexagonal plates are observed at temperatures lower than -12°C. This suggests that heterogeneous nucleation is occurring within the stratiform cloud region (Bailey and Hallett 2009), as if they were formed via homogeneous nucleation they would have grown to larger sizes (via aggregation and/or deposition), and would most likely have a more complex crystal shape. We are unable to determine the extent to which heterogeneous nucleation is occurring as it requires an accurate image classification scheme, which we do not have at present. As already mentioned, large numbers of column ice particles are observed near the NCFR.

Figure 9 also shows that near the NCFR, but at slightly lower temperatures (approx. -12°C), capped columns are observed. We argue that these are columns which have formed in the HM region and have been transported vertically upwards in the updraught. As they are lifted above the -8°C level, they enter an environment favouring plate-like growth (Bailey and Hallett 2009). This leads to the formation of plates on the ends of the columns. These capped-columns are found in the region of high Z_{DR} identified by CAMRa; this region had a horizontal extent of ~30 km horizontal extent and a vertical thickness of only a few hundred meters. It appears this high Z_{DR}/capped-column region is some form of outflow from the top of the NCFR (analogous to anvil cirrus in regions of deep convection, albeit embedded within stratiform cloud). Based on the Z_{DR} data shown in Figure 5e, this layer appears to advect faster than the NCFR itself, likely due to wind shear in the vertical.

Wolde and Vali (2001) show that regions of capped columns mixed with pristine plates do result in a detectable signal in Z_{DR} (~1.5) at near horizontal beam angles. This signal in Z_{DR} is small in comparison to that for pristine plates alone (~6). There are no measurements of Z_{DR} for isolated pristine capped columns available in the literature.

3.4.4 Probe Inter-arrival time analysis

In order to remove shattering artefacts from the CIP-15 and CIP-100 probes, histograms of particle inter-arrival time were examined. Examples are shown in Figures 10 and 11 for the CIP-15 and CIP-100 respectively. These histograms were constructed for the same time periods as the size distributions in Figure 8. IAT histograms are not shown for -56°C and -25°C as they largely replicate those for -42°C. Also shown in Figures 10 and 11 are mean particle size in each IAT bin (using the area equivalent diameter), and the CDF of the number concentration. These are added to provide an indication of the typical size of particle in each IAT mode/bin, and the relative contribution of each mode in the IAT histogram to the total number concentration.

The CIP-15 generally shows bimodal spectra with a shattering mode to the left, centred just below $1\text{x}10^{-5}$ s, and another mode of particles to the right. The right hand mode located at ~$2\text{x}10^{-3}$ s in 9a-9c represents intact (i.e. non-shattering) particles and does not generally extend below 10^{-4} s, making this a suitable choice as an IAT threshold in these regions. The shattered particles below the IAT threshold can contribute significantly to the number concentration (e.g. > 80% at -18°C as in Figure 10b), and so must be removed to avoid contamination. This strict thresholding method may remove a small number of valid particles, but the IAT histograms show these erroneously filtered particles only have a small contribution to the total number concentration.

Figure 10d is from the NCFR where HM multiplication is acting to increase the ambient ice particle concentration. The large concentrations observed here cause a shift in the mode of the valid particles to the left, centred at ~$2x10^{-4}$ s. Due to this shift and the width of the mode, a large number of valid particles are pushed below the previously acceptable IAT threshold of 10^{-4} s. A threshold of 10^{-5} s is more appropriate in this region. Note the relative number of intact particles greatly exceeds the shattered ones in the HM multiplication zone, and near cloud top.

The CIP-100 shows modest signs of bi-modality (and hence shattering) at the lower temperatures (Figures 11a-b). At these levels, particles with an IAT<10^{-4} s contribute around 15% to the total number concentration measured. However, Figure 10c shows a more pronounced shattering mode, with contaminations of approximately 50% to the number concentration with an IAT < 10^{-4} s. In the NCFR where HM multiplication was observed (Figure 11d), the shattering mode is engulfed by valid particle counts. This is due to a shift to the left as the ambient particle concentration increases by over an order of magnitude relative to the region shown in Figure 11c. Using an IAT threshold of 10^{-4} s in the NCFR region leads to the reduction of the number concentration by 90%, when most of these particles are valid. A more modest IAT threshold of 10^{-5} s in this region results in a loss of only 10% of the particles.

In order to take into account this variability in the IAT threshold, a preliminary stage of data processing was conducted with an IAT threshold of 10^{-4} s. As discussed above, this is at times too large and will lead to a negative bias in the reported concentrations (especially for the CIP-100 in the HM zone). After the preliminary processing, periods identified to have high number concentrations (> 20 L^{-1}) were reprocessed with a new IAT of 10^{-5} s to reduce this negative bias. The result of this was a significant improvement between the CIP-15 and CIP-100 in the overlap region, by allowing more counts in the lower size bins of the CIP-100 in the HM zone. The agreement between the probes in the other regions of the cloud was unaltered by this modified IAT threshold. This IAT filtering was implemented for all the analysis shown in this paper. It should be noted that using IAT filtering on OAP may not remove all shattering artefacts (Korolev et al,. 2011), and so some shattering artefacts may still be present.

The influence of shattering artefacts on other published datasets needs to be understood. Particle IAT analyses should be conducted on key datasets when particle time stamp information is available. When this information is not available, data below a certain size (nominally 300 µm) should be discarded. The shattering characteristics for different probes need to be understood. Shattering artefacts should be minimised before they affect data, instead of relying on post processing techniques. Therefore, using modified probe tips as described by Korolev et al (2011, 2012) is highly recommended.

3.5 Summary of the NCFR

Ice multiplication appears to be active in the NCFR as it has all the necessary requirements. Convection is driven from near the surface due to the movement and strength of the cold front. Significant amounts of supercooled liquid water are generated as a result. We also have stratiform precipitation/snow from the larger scale slantwise ascent of the system as a whole, as well as that produced at cloud top in convectively generated fallstreaks. Combining the liquid water source and the stratiform precipitation with favourable thermodynamic conditions (i.e. suitable cloud base temperature) leads to a scenario where the HM process is highly active. We have attempted to visualise this scenario in Figure 12. The splinters produced can either aggregate/rime and precipitate out of the rainband, or are transported vertically upwards into an outflow region and develop into capped columns.

4. Conclusions

We have presented in-situ and remote sensing measurements in a cold frontal system. The system was found to contain a Narrow Cold Frontal Rainband (NCFR), embedded within a Wide Cold Frontal Rainband (WCFR). A summary of our conclusions follows:

- The effects of ice multiplication were observed in the vicinity of the NCFR, resulting in the highest ice particle number concentrations being observed at temperatures > -10°C. This was most likely due to the rime splintering process as described by Mossop and Hallett (1974). Evidence supporting this lies in the ice particle number concentrations (> 100 L^{-1}), particle sizes (~400 µm), particle habit (pristine columns), and location (proximity to the NCFR and the -3°C to -8°C isotherms).

- Ice multiplication occurred due to the generation of supercooled liquid water along the convective NCFR. The convection spanned the region where rime splintering is known to be active (-3°C to -8°C). Snow particles from the stratiform region appear to be rimed near the NCFR, with no evidence of graupel. This suggests that rime splintering results from the interaction of the NCFR and stratiform precipitation (and not graupel), and that snow particles are acting as sites for rime splintering. This was also shown by Marwitz (1987). We cannot rule out the presence of graupel in regions we did not sample, such as in the regions of peak radar reflectivity.

- Particles generated via multiplication accounted for a significant fraction of the ice water content (~15%). These particles will precipitate slowly due to their small size, altering the precipitation budget of the system and the pattern of latent heat release.

- Some ice particles resulting from the multiplication process were transported out of the convective feature by the updraught, forming an elevated layer of ice crystals. These particles had entered a new growth regime, and evolved from pristine columns into capped columns. This elevated layer from the convective outflow was identifiable in the radar differential reflectivity data.

- Available parameterizations which diagnose the cloud particle size distribution do not represent the effects of rime splintering. Most parameterizations are functions of temperature alone. More sophisticated parameterizations use multiple parameters, but still do not include the effects of ice multiplication.

- The presence of secondary ice and mixed phase conditions require modifications to artefact removal from imaging probes when considering particle inter-arrival time analysis. This has impacts on both medium (e.g. CIP-15) and coarse (e.g. CIP-100) resolution imaging probes. The use of anti-shatter tips on imaging probes, as described by Korolev et al (2011), reduces these complications and is recommended, as inter-arrival time analysis has shown to be less effective at removing artefacts than modified probe designs.

- The majority of primary ice particles were generated close to cloud top by homogeneous and heterogeneous nucleation. These were often associated with convective elements identified by the radar and lead to fall streaks of growing and aggregating ice crystals.

- The relative role of homogeneous and heterogeneous ice nucleation on the formation of the stratiform precipitation cannot be quantified, but it is likely that homogeneous nucleation is occurring at temperatures below -35°C, and heterogeneous nucleation throughout the depth of the cloud.

- Model studies are required to quantify the roles of homogeneous, heterogeneous and secondary ice formation mechanisms on precipitation formation in NCFRs in a variety of conditions (dynamical, thermo-dynamical, and microphysical). The feedback on dynamics via alterations to latent heating patterns should also be explored.

Acknowledgements

This work was funded by the NERC APPRAISE programme, grant number NE/E01125X/1. We would like to acknowledge the support from FGAM, FAAM and Direct Flight in obtaining the aircraft dataset. We would also like to thank the following for supporting the CFARR measurements: Andrew Barrett (University of Reading), Darcy Ladd and Charles Wrench (CFARR). Operational analysis fields were obtained from the ECMWF data archive (http://data.ecmwf.int/data/). We would like to acknowledge the UK Met Office for the CIP-100 data. The Meteosat image and operational radar data were obtained from the British Atmospheric Data Centre (BADC) online archive.

References

Agusti-Panareda, A., Gray, S. L., & Belcher, S. E. (2009). On the dependence of boundary layer ventilation on frontal type. J. Geophys. Res., 114(D5), D05305. doi:10.1029/2008JD010694

Bailey, M. P., & Hallett, J. (2009). A Comprehensive Habit Diagram for Atmospheric Ice Crystals: Confirmation from the Laboratory, AIRS II, and Other Field Studies. Journal of the Atmospheric Sciences, 66(9), 2888–2899. doi:10.1175/2009JAS2883.1

Baumgardner, D., Jonsson, H., Dawson, W., O'Connor, D., & Newton, R. (2001). The cloud, aerosol and precipitation spectrometer: a new instrument for cloud investigations. Atmospheric Research, 59–60(0), 251–264. doi:10.1016/S0169-8095(01)00119-3

Brown, P. R. A., & Francis, P. N. (1995). Improved Measurements of the Ice Water Content in Cirrus Using a Total-Water Probe. Journal of Atmospheric and Oceanic Technology, 12(2), 410–414. doi:10.1175/1520-0426(1995)012<0410:IMOTIW>2.0.CO;2

Browning, Keith A. (1986). Conceptual Models of Precipitation Systems. Weather and Forecasting, 1(1), 23–41. doi:10.1175/1520-0434(1986)001<0023:CMOPS>2.0.CO;2

Browning, K. A., & Reynolds, R. (1994). Diagnostic study of a narrow cold-frontal rainband and severe winds associated with a stratospheric intrusion. Quarterly Journal of the Royal Meteorological Society, 120(516), 235–257. Retrieved from http://dx.doi.org/10.1002/qj.49712051602

Browning, K. A., & Roberts, N. M. (1996). Variation of frontal and precipitation structure along a cold front. Quarterly Journal of the Royal Meteorological Society, 122(536), 1845–1872. doi:10.1002/qj.49712253606

Bower, K. N., Moss, S. J., Johnson, D. W., Choularton, T. W., Latham, J., Brown, P. R. A., Blyth, A. M., et al. (1996). A parametrization of the ice water content observed in frontal and convective clouds. Quarterly Journal of the Royal Meteorological Society, 122(536), 1815–1844. doi:10.1002/qj.49712253605

Chapman, D., & Browning, K. A. (1998). Use of wind-shear displays for Doppler radar data. Bulletin of the American Meteorological Society, 79(12), 2685-2691

Crawford, I., Bower, K. N., Choularton, T. W., Dearden, C., Crosier, J., Westbrook, C., Capes, G., et al. (2012). Ice formation and development in aged, wintertime cumulus over the UK: observations and modelling. Atmospheric Chemistry and Physics, 12(11), 4963–4985. doi:10.5194/acp-12-4963-2012

Crosier, J., Bower, K. N., Choularton, T. W., Westbrook, C. D., Connolly, P. J., Cui, Z. Q., Crawford, I. P., et al. (2011). Observations of ice multiplication in a weakly convective cell embedded in supercooled mid-level stratus. Atmospheric Chemistry and Physics, 11(1), 257–273. doi:10.5194/acp-11-257-2011

Cui, Z., Blyth, A. M., Bower, K. N., Crosier, J., & Choularton, T. (2012). Aircraft measurements of wave clouds. Atmos. Chem. Phys., 12(20), 9881–9892. doi:10.5194/acp-12-9881-2012

Field, P. R. (2000). Bimodal ice spectra in frontal clouds. Quarterly Journal of the Royal Meteorological Society, 126(563), 379–392. Retrieved from http://dx.doi.org/10.1002/qj.49712656302

Field, P R, Hogan, R. J., Brown, P. R. A., Illingworth, A. J., Choularton, T. W., & Cotton, R. J. (2005). Parametrization of ice-particle size distributions for mid-latitude stratiform cloud. Quarterly Journal of the Royal Meteorological Society, 131(609), 1997–2017. Retrieved from http://dx.doi.org/10.1256/qj.04.134

Field, P. R., Heymsfield, A. J., & Bansemer, A. (2006). Shattering and Particle Interarrival Times Measured by Optical Array Probes in Ice Clouds. Journal of Atmospheric and Oceanic Technology, 23(10), 1357–1371. doi:10.1175/JTECH1922.1

Field, Paul R, Heymsfield, A. J., & Bansemer, A. (2007). Snow Size Distribution Parameterization for Midlatitude and Tropical Ice Clouds. Journal of the Atmospheric Sciences, 64(12), 4346–4365. doi:10.1175/2007JAS2344.1

Goddard, J. W. F., Eastment, J. D., & Tan, J. (1994). Self-consistent measurements of differential phase and differential reflectivity in rain. Geoscience and Remote Sensing Symposium, 1994. IGARSS '94. Surface and Atmospheric Remote Sensing: Technologies, Data Analysis and Interpretation., International (Vol. 1, pp. 369 –371 vol.1). doi:10.1109/IGARSS.1994.399128

Hallett, J., & Mossop, S. C. (1974). Production of secondary ice particles during the riming process. Nature, 249(5452), 26–28. Retrieved from http://dx.doi.org/10.1038/249026a0

Heymsfield, A. J., Bansemer, A., & Twohy, C. H. (2007). Refinements to Ice Particle Mass Dimensional and Terminal Velocity Relationships for Ice Clouds. Part I: Temperature Dependence. Journal of the Atmospheric Sciences, 64(4), 1047–1067. doi:10.1175/JAS3890.1

Heymsfield, A. J., & Parrish, J. L. (1978). A Computational Technique for Increasing the Effective Sampling Volume of the PMS Two-Dimensional Particle Size Spectrometer. Journal of Applied Meteorology, 17(10), 1566–1572. doi:10.1175/1520-0450(1978)017<1566:ACTFIT>2.0.CO;2

Heymsfield, A. J., Schmitt, C., Bansemer, A., & Twohy, C. H. (2010). Improved Representation of Ice Particle Masses Based on Observations in Natural Clouds. Journal of the Atmospheric Sciences, 67(10), 3303–3318. doi:10.1175/2010JAS3507.1

Hobbs, P. V., & Persson, P. O. G. (1982). The Mesoscale and Microscale Structure and organization of Clouds and precipitation in Midlatitude Cyclones. Part V: The Substructure of Narrow Cold-Frontal Rainbands. Journal of the Atmospheric Sciences, 39(2), 280–295. doi:10.1175/1520-0469(1982)039<0280:TMAMSA>2.0.CO;2

Hogan, R. J., Field, P. R., Illingworth, A. J., Cotton, R. J., & Choularton, T. W. (2002). Properties of embedded convection in warm-frontal mixed-phase cloud from aircraft and polarimetric radar. Quarterly Journal of the Royal Meteorological Society, 128(580), 451–476. doi:10.1256/003590002321042054

Hogan, R. J., Mittermaier, M. P., & Illingworth, A. J. (2006). The Retrieval of Ice Water Content from Radar Reflectivity Factor and Temperature and Its Use in Evaluating a Mesoscale Model. Journal of Applied Meteorology and Climatology, 45(2), 301–317. doi:10.1175/JAM2340.1

James, P. K., & Browning, K. A. (1979). Mesoscale structure of line convection at surface cold fronts. Quarterly Journal of the Royal Meteorological Society, 105(444), 371–382. doi:10.1002/qj.49710544404

Jorgensen, D. P., Pu, Z., Persson, P. O. G., & Tao, W.-K. (2003). Variations Associated with Cores and Gaps of a Pacific Narrow Cold Frontal Rainband. Monthly Weather Review, 131(11), 2705–2729. doi:10.1175/1520-0493(2003)131<2705:VAWCAG>2.0.CO;2

Korolev, A., Emery, E., & Creelman, K. (2012). Modification and Tests of Particle Probe Tips to Mitigate Effects of Ice Shattering. Journal of Atmospheric and Oceanic Technology, 30(4), 690–708. doi:10.1175/JTECH-D-12-00142.1

Korolev, A. V., Emery, E. F., Strapp, J. W., Cober, S. G., Isaac, G. A., Wasey, M., & Marcotte, D. (2011). Small Ice Particles in Tropospheric Clouds: Fact or Artifact? Airborne Icing Instrumentation Evaluation Experiment. Bulletin of the American Meteorological Society, 92(8), 967–973. doi:10.1175/2010BAMS3141.1

Korolev, A. (2007). Reconstruction of the Sizes of Spherical Particles from Their Shadow Images. Part I: Theoretical Considerations. Journal of Atmospheric and Oceanic Technology, 24(3), 376–389. doi:10.1175/JTECH1980.1

Korolev, A. V, & Mazin, I. P. (2003). Supersaturation of Water Vapor in Clouds. Journal of the Atmospheric Sciences, 60(24), 2957–2974. doi:10.1175/1520-0469(2003)060<2957:SOWVIC>2.0.CO;2

Lance, S., Brock, C. A., Rogers, D., & Gordon, J. A. (2010). Water droplet calibration of the Cloud Droplet Probe (CDP) and in-flight performance in liquid, ice and mixed-phase clouds during ARCPAC. Atmospheric Measurement Techniques, 3(6), 1683–1706. doi:10.5194/amt-3-1683-2010

Lawson, R. P., O'Connor, D., Zmarzly, P., Weaver, K., Baker, B., Mo, Q., & Jonsson, H. (2006). The 2D-S (Stereo) Probe: Design and Preliminary Tests of a New Airborne, High-Speed, High-Resolution Particle Imaging Probe. Journal of Atmospheric and Oceanic Technology, 23(11), 1462–1477. doi:10.1175/JTECH1927.1

Locatelli, J. D., & Hobbs, P. V. (1974). Fall speeds and masses of solid precipitation particles. Journal of Geophysical Research, 79(15), 2185–2197. doi:10.1029/JC079i015p02185

Locatelli, J. D., Martin, J. E., & Hobbs, P. V. (1995). Development and propagation of precipitation cores on cold fronts. Atmospheric Research, 38(1–4), 177–206. Retrieved from http://www.sciencedirect.com/science/article/pii/016980959400093S

Marwitz, J. D. (1987). Deep Orographic Storms over the Sierra Nevada. Part II: The Precipitation Processes. Journal of the Atmospheric Sciences, 44(1), 174–185. doi:10.1175/1520-0469(1987)044<0174:DOSOTS>2.0.CO;2

Matejka, T. J., Houze, R. A., & Hobbs, P. V. (1980). Microphysics and dynamics of clouds associated with mesoscale rainbands in extratropical cyclones. Quarterly Journal of the Royal Meteorological Society, 106(447), 29–56. doi:10.1002/qj.49710644704

Norbury, J. R., & White, W. J. (1971). A rapid-response rain gauge. (W. J. White, Ed.) Journal of Physics E: Scientific Instruments, 4(8), 601

Rutledge, S. A., & Hobbs, P. V. (1984). The Mesoscale and Microscale Structure and Organization of Clouds and Precipitation in Midlatitude Cyclones. XII: A Diagnostic Modeling Study of Precipitation Development in Narrow Cold-Frontal Rainbands. Journal of the Atmospheric Sciences, 41(20), 2949–2972. doi:10.1175/1520-0469(1984)041<2949:TMAMSA>2.0.CO;2

Stoelinga, M. T., Hobbs, P. V., Mass, C. F., Locatelli, J. D., Colle, B. A., Houze, R. A., Rangno, A. L., et al. (2003). Improvement of Microphysical Parameterization through Observational Verification Experiment. Bulletin of the American Meteorological Society, 84(12), 1807–1826. doi:10.1175/BAMS-84-12-1807

Westbrook, C. D., & Illingworth, A. J. (2011). Evidence that ice forms primarily in supercooled liquid clouds at temperatures > -27°C. Geophys. Res. Lett., 38(14), L14808. doi:10.1029/2011GL048021

Wolde, M., & Vali, G. (2001). Polarimetric Signatures from Ice Crystals Observed at 95 GHz in Winter Clouds. Part I: Dependence on Crystal Form. Journal of the Atmospheric Sciences, 58(8), 828–841. doi:10.1175/1520-0469(2001)058<0828:PSFICO>2.0.CO;2

Woods, C. P., Stoelinga, M. T., & Locatelli, J. D. (2008). Size Spectra of Snow Particles Measured in Wintertime Precipitation in the Pacific Northwest. Journal of the Atmospheric Sciences, 65(1), 189–205. doi:10.1175/2007JAS2243.1

Figure Captions

Figure 1: ECMWF operational analysis (0.25° resolution) for 1800 UTC on 3 March 2009. (a) Equivalent potential temperature (θ_e) on the 500 hPa pressure level in colour, and white lines (3 hPa spacing, 972 hPa minimum contour) for mean sea level pressure contours. Also highlighted are the location of the CFARR ground site (black cross) and 51.24° latitude (dashed line). (b) Vertical slice of θ_e and (c) relative humidity along 51.24° latitude.

Figure 2: Meteosat Second Generation (MSG) infrared image (10.8 μm), 1800 UTC on 3 March 2009.

Figure 3: Precipitation rate estimated from UK operational radar network (NIMROD dataset) for (a,d) 1800 UTC, (b,e) 1900 UTC and (c,f) 2000 UTC on 3 March 2009. The locations of domains for (d-f) are marked on (a-c). Axis ticks on (a-c) and (d-f) (i.e. $\Delta_{x,y}$) are 150 and 20 km apart respectively. The location of the CFARR ground site is marked in (d-f) with a red circle. Minimum detectable rainfall rates are ~0.03 mm hour^{-1}, Regions within range of the radar network, but with no detectable signal are coloured gray.

Figure 4: Surface observations from the CFARR ground site of (a) temperature, relative humidity, (b) (b) wind speed, wind direction, (c) precipitation rate and surface pressure.

Figure 5: RHI scan of (a) Radar Reflectivity (dBZ_h), (b) unfolded Doppler velocity (v_u), (c) Differential Reflectivity (Z_{DR}) and (d) vertical velocity (w) from the 3-GHz radar (CAMRa). The scan was performed between 19:22:07 - 19:23:07. The radar reflectivity factor was obtained from the horizontally polarised beam. The BAe-146 flight track (19:09:00 -

19:27:36) is marked on (a)-(d) with a black line. Shown in (e) are in-situ number concentrations and the second moment of the PSD (left and right axis respectively) from the merged CIP-15/100 data. Also shown in (f) are radar reflectivities obtained along the flight track from CAMRa and that calculated from the in-situ data. The x-axes are reversed (conventionally showing east to the right, west to the left) as the scan was performed along the 255° radial. Note the detection limit of dBZ_h = -20 at 10 km, which rises to dBZ_h = 0 at 100 km range. Positive Doppler velocities represent motion towards the radar.

Figure 6: As figure 5 for panels (a) and (b), but for the RHI scan spanning the time 20:03:24 – 20:04:23, and for flight times 19:58:00 – 20:08:00. Total particle number concentration (left axis) and second moment of size distribution (right axis) in-situ data are shown in (c). Measured (CAMRa) and calculated (in-situ data) Radar Reflectivty are shown in (d).

Figure 7: Vertical profile of (a) number concentration, (b) mean diameter, (c) second moment of the PSD and (d) ambient temperature. The merged CIP-15/100 data are used for (a)-(c), and the Rosemount de-iced temperature sensor data for (d). Altitude bins are 500 m wide. Dark shading, light shading and white circles represent Inter-quartile range, 25th/75th to 0th/100th percentile range, and median values respectively. Vertical profiles of Radar Reflectivity at distances of +20, +10, 0 and -10 km relative to the rainband (positive values are closer to CFARR) are shown in (e). A comparison of measured (from CAMRa) and calculated (from in-situ data) is shown in (f), with datapoints coloured according to ambient temperature.

Figure 8: Size distributions of number concentration from the CIP-15 (black) and CIP-100 (grey) onboard the BAe-146. Also shown in green are curves using parameterizations of the size distribution. Cumulative Distribution Frequency (CDF) curves for the number concentration (blue) and second moment (red) are plotted on the right axis as a function of increasing particle diameter (D_p).

Figure 9: Example particle images from the 2D-S probe as observed in the different temperature/process regions of the cloud.

Figure 10: Particle inter-arrival time histograms (black, right axis) for the CIP-15 at -42°C, -18°C and from within and outside the NCFR regions at -10°C (a-d) respectively. Also shown are the mean area equivalent diameter (blue) and the cumulative distribution function (CDF) of the number concentration (red).

Figure 11: Particle inter-arrival time histograms (black, right axis) for the CIP-100 at -42°C, -18°C and from within and outside the NCFR regions at -10°C (a-d) respectively. Also shown are the mean area equivalent diameter (blue) and the cumulative distribution function (CDF) of the number concentration (red).

Figure 12: Schematic of microphysical processes controlling ice number concentration and precipitation formation in a Narrow Cold Frontal Rainband.

Figures

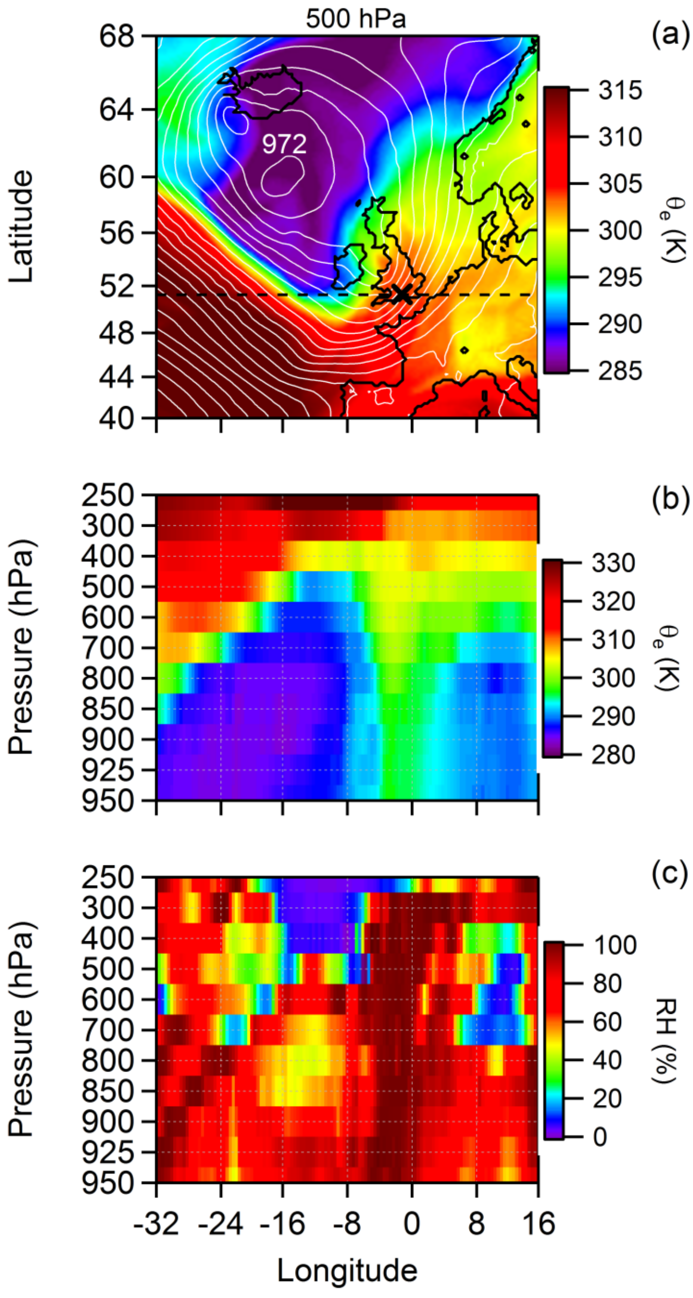

Figure 1: ECMWF operational analysis (0.25° resolution) for 1800 UTC on 3 March 2009. (a) Equivalent potential temperature (θ_e) on the 500 hPa pressure level in colour, and white lines (3 hPa spacing, 972 hPa minimum contour) for mean sea level pressure contours. Also highlighted are the location of the CFARR ground site (black cross) and 51.24° latitude (dashed line). (b) Vertical slice of θ_e and (c) relative humidity along 51.24° latitude.

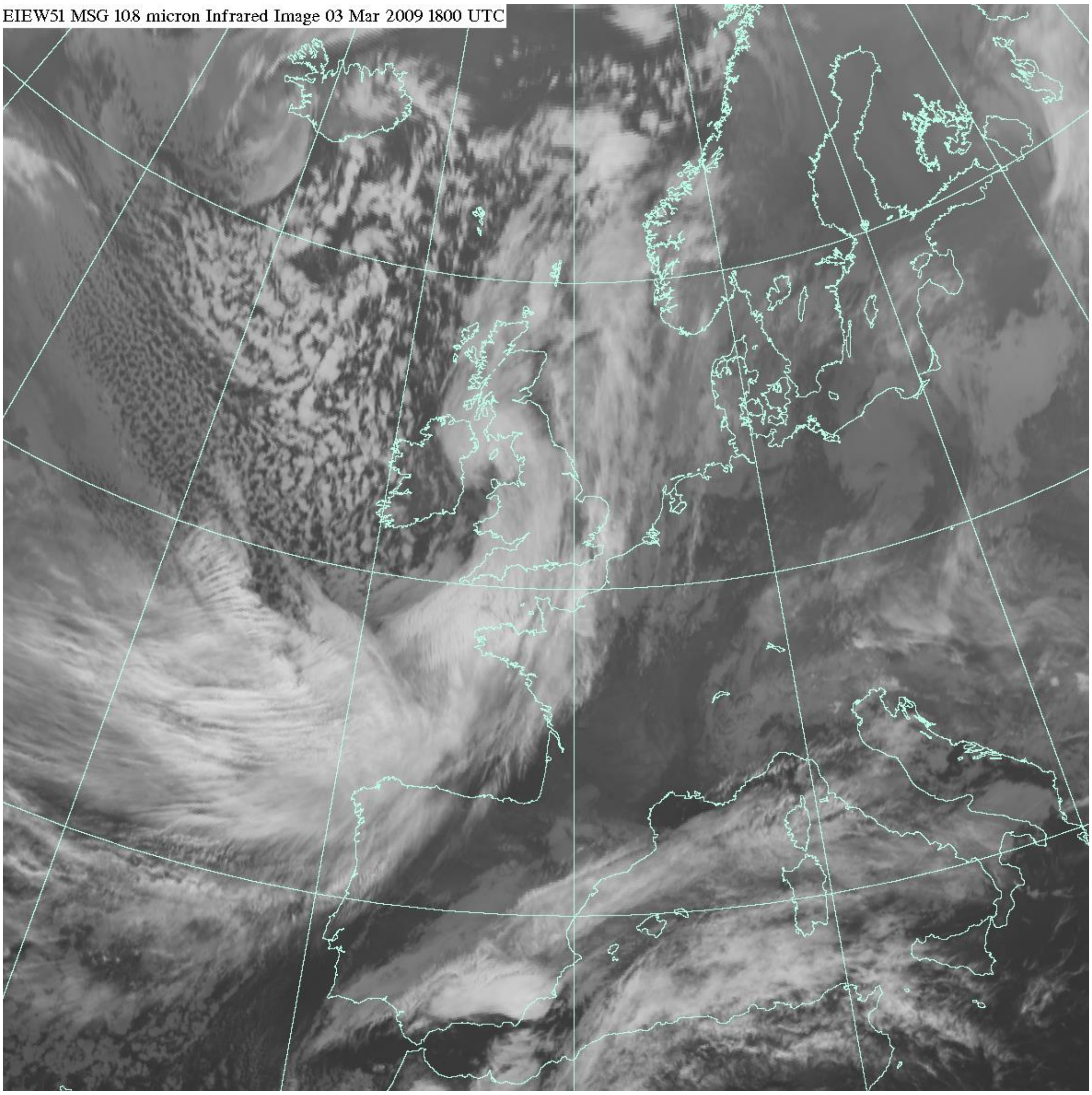

Figure 2: Meteosat Second Generation (MSG) infrared image (10.8 μm), 1800 UTC on 3 March 2009.

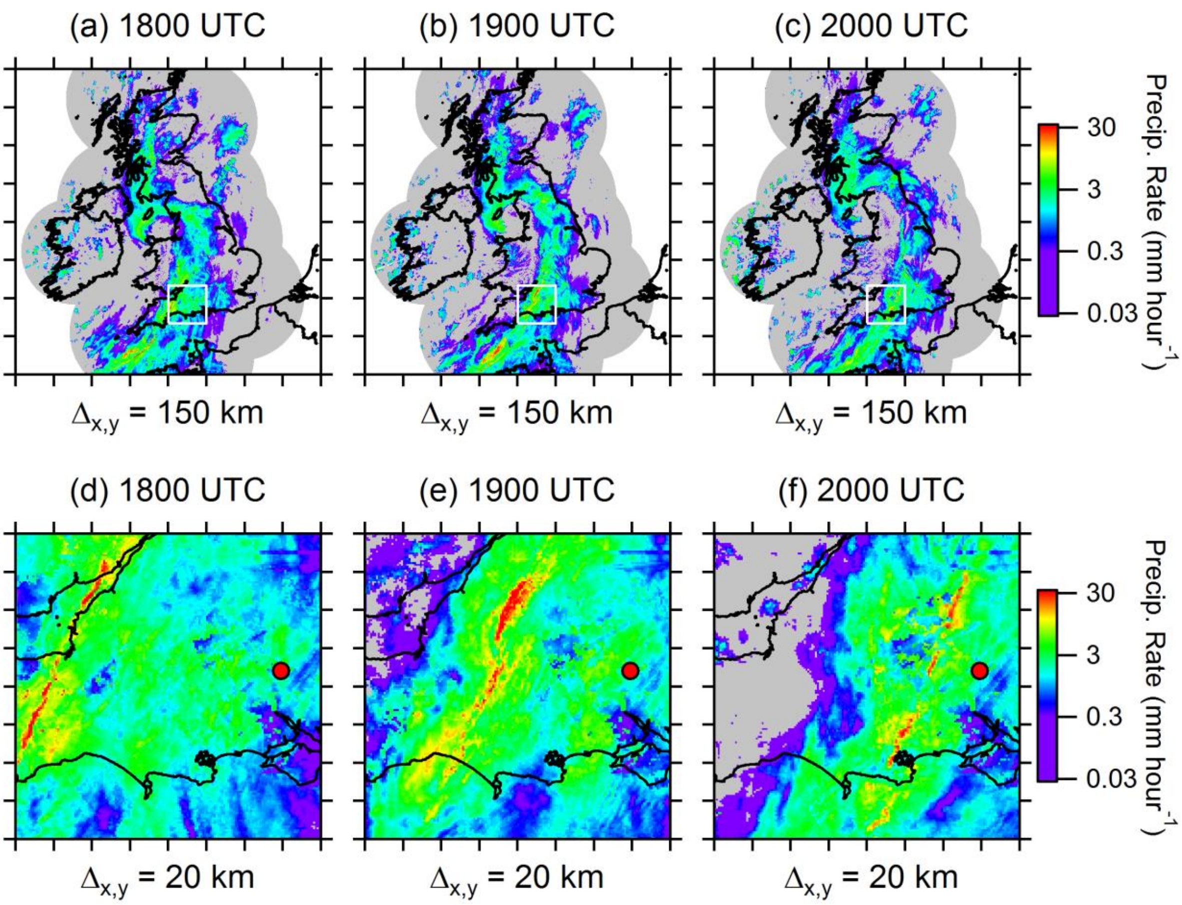

Figure 3: Precipitation rate estimated from UK operational radar network (NIMROD dataset) for (a,d) 1800 UTC, (b,e) 1900 UTC and (c,f) 2000 UTC on 3 March 2009. The locations of domains for (d-f) are marked on (a-c). Axis ticks on (a-c) and (d-f) (i.e. $\Delta_{x,y}$) are 150 and 20 km apart respectively. The location of the CFARR ground site is marked in (d-f) with a red circle. Minimum detectable rainfall rates are ~0.03 mm hour^{-1}, Regions within range of the radar network, but with no detectable signal are coloured gray.

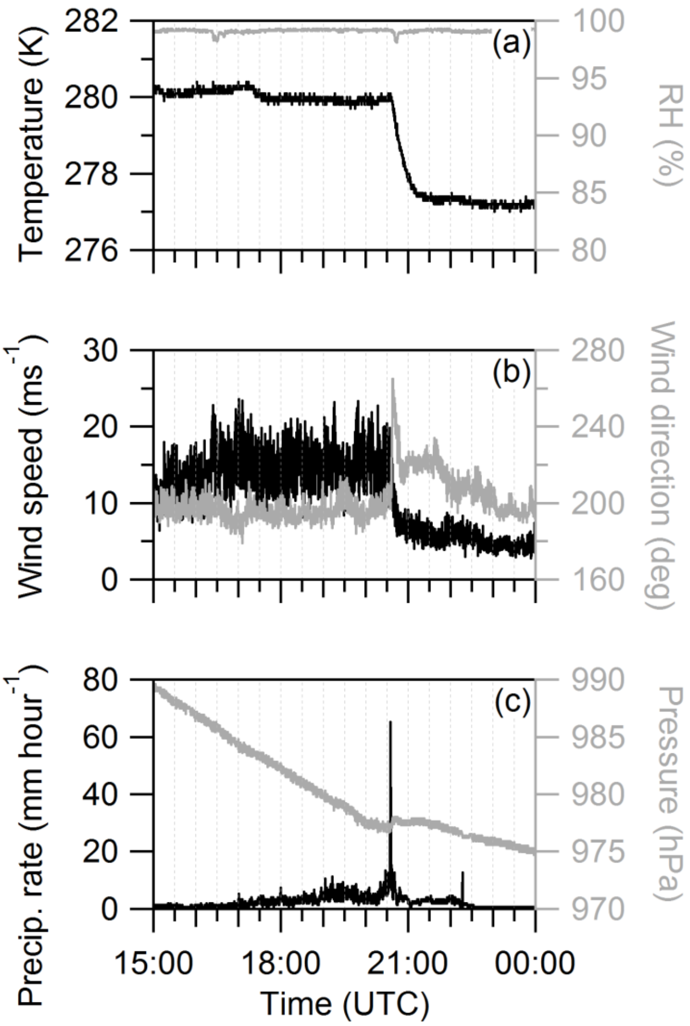

Figure 4: Surface observations from the CFARR ground site of (a) temperature, relative humidity, (b) (b) wind speed, wind direction, (c) precipitation rate and surface pressure.

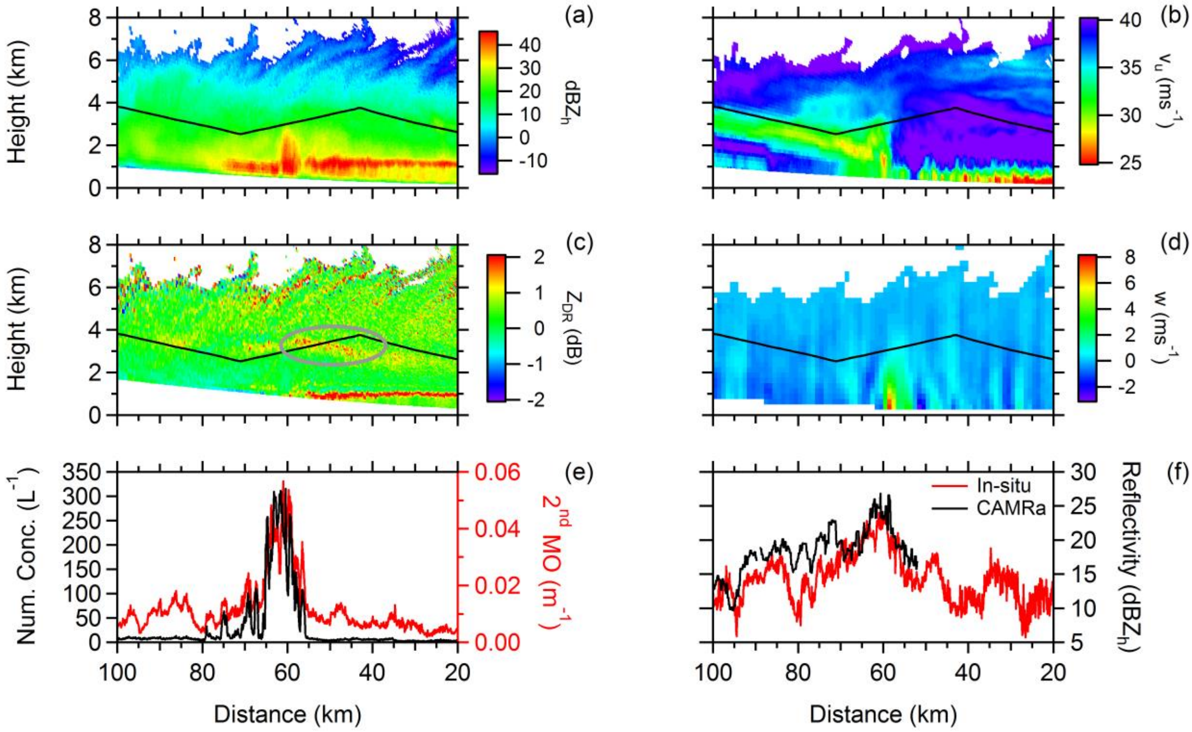

Figure 5: RHI scan of (a) Radar Reflectivity (dBZ$_h$), (b) unfolded Doppler velocity (v_u), (c) Differential Reflectivity (Z_{DR}) and (d) vertical velocity (w) from the 3-GHz radar (CAMRa). The scan was performed between 19:22:07 - 19:23:07. The radar reflectivity factor was obtained from the horizontally polarised beam. The BAe-146 flight track (19:09:00 - 19:27:36) is marked on (a)-(d) with a black line. Shown in (e) are in-situ number concentrations and the second moment of the PSD (left and right axis respectively) from the merged CIP-15/100 data. Also shown in (f) are radar reflectivities obtained along the flight track from CAMRa and that calculated from the in-situ data. The x-axes are reversed (conventionally showing east to the right, west to the left) as the scan was performed along the 255° radial. Note the detection limit of dBZ$_h$ = -20 at 10 km, which rises to dBZ$_h$ = 0 at 100 km range. Positive Doppler velocities represent motion towards the radar.

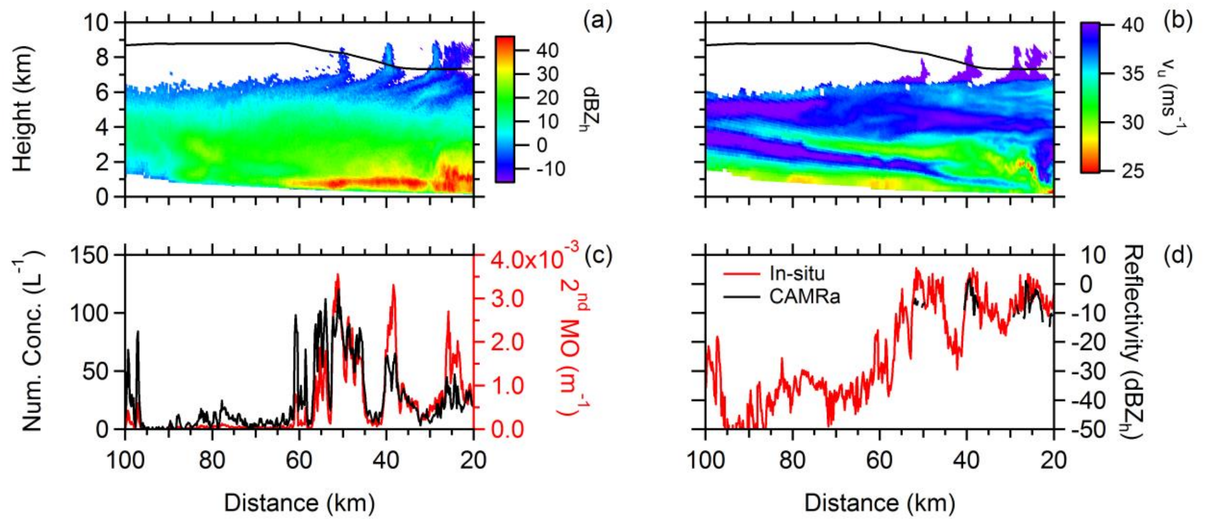

Figure 6: As figure 5 for panels (a) and (b), but for the RHI scan spanning the time 20:03:24 – 20:04:23, and for flight times 19:58:00 – 20:08:00. Total particle number concentration (left axis) and second moment of size distribution (right axis) in-situ data are shown in (c). Measured (CAMRa) and calculated (in-situ data) Radar Reflectivty are shown in (d).

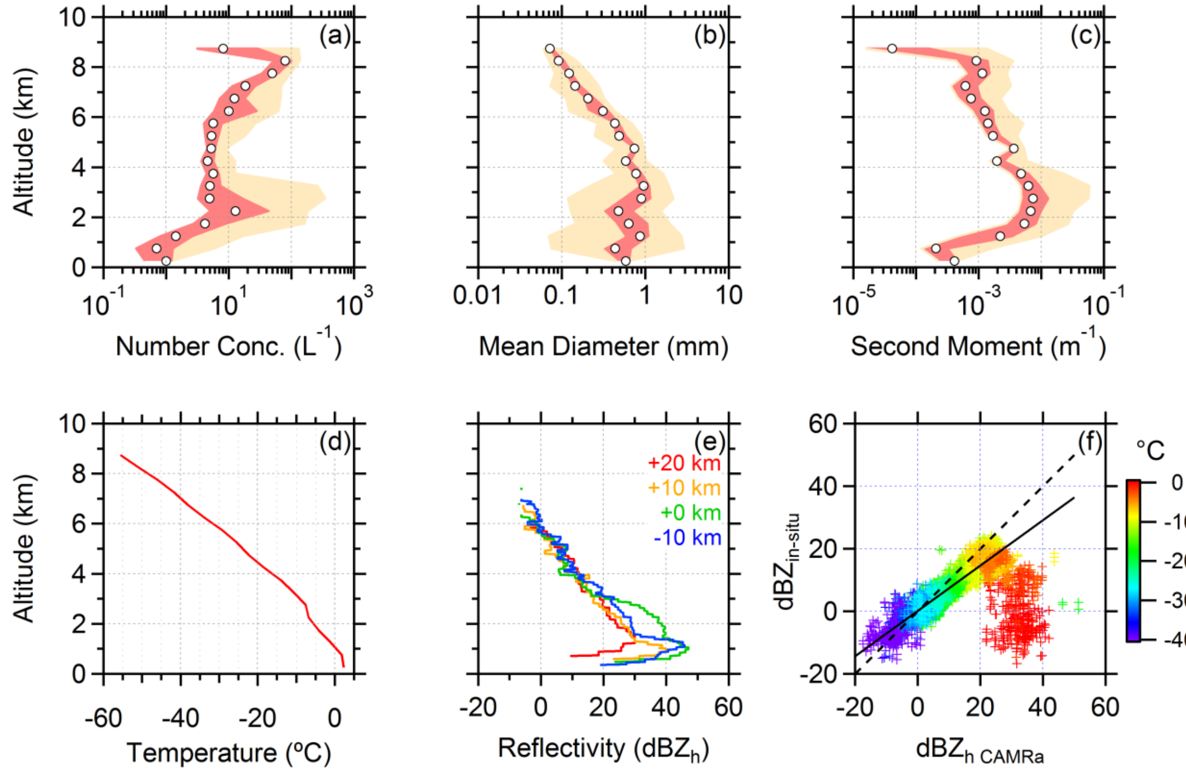

Figure 7: Vertical profile of (a) number concentration, (b) mean diameter, (c) second moment of the PSD and (d) ambient temperature. The merged CIP-15/100 data are used for (a)-(c), and the Rosemount de-iced temperature sensor data for (d). Altitude bins are 500 m wide. Dark shading, light shading and white circles represent Inter-quartile range, $25^{th}/75^{th}$ to $0^{th}/100^{th}$ percentile range, and median values respectively. Vertical profiles of Radar Reflectivity at distances of +20, +10, 0 and -10 km relative to the rainband (positive values are closer to CFARR) are shown in (e). A comparison of measured (from CAMRa) and calculated (from in-situ data) is shown in (f), with datapoints coloured according to ambient temperature.

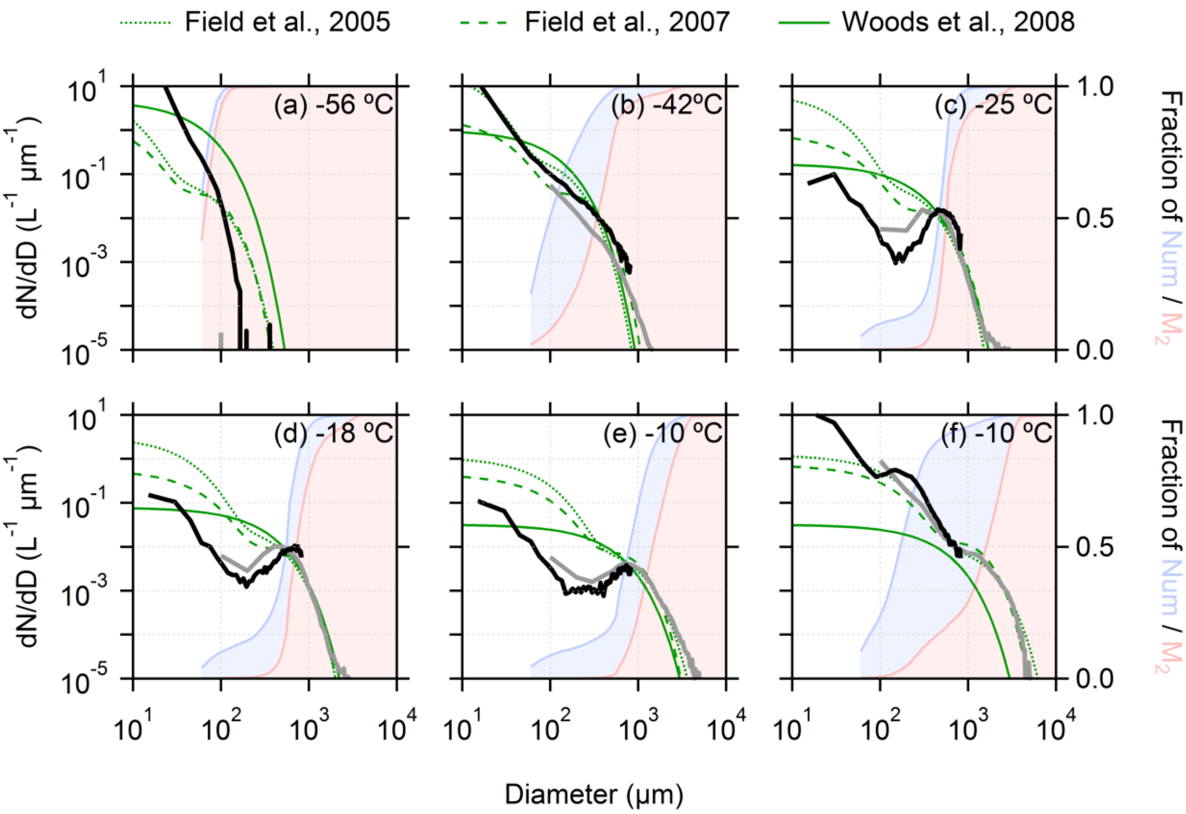

Figure 8: Size distributions of number concentration from the CIP-15 (black) and CIP-100 (grey) onboard the BAe-146. Also shown in green are curves using parameterizations of the size distribution. Cumulative Distribution Frequency (CDF) curves for the number concentration (blue) and second moment (red) are plotted on the right axis as a function of increasing particle diameter (D_p).

937

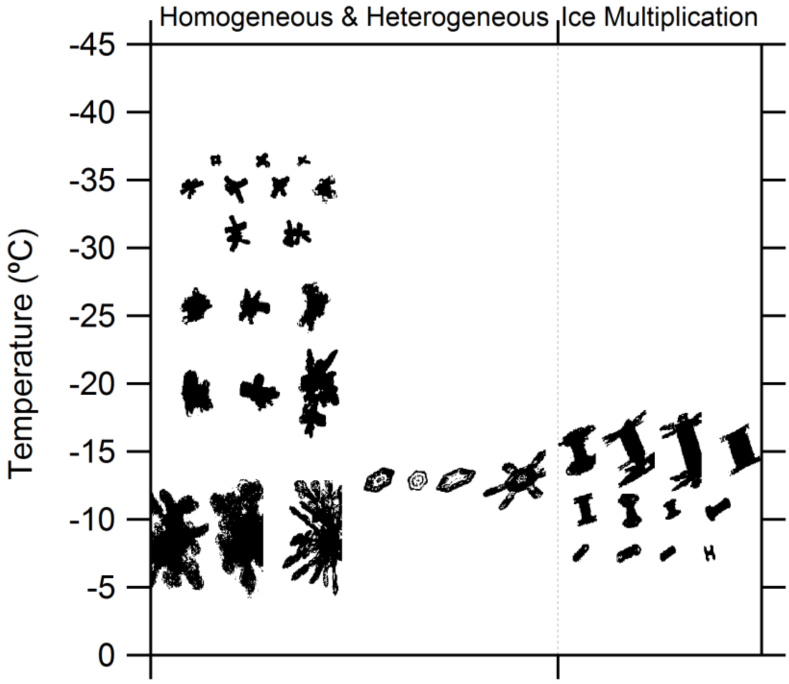

938

939 Figure 9: Example particle images from the 2D-S probe as observed in the different

940 temperature/process regions of the cloud.

941

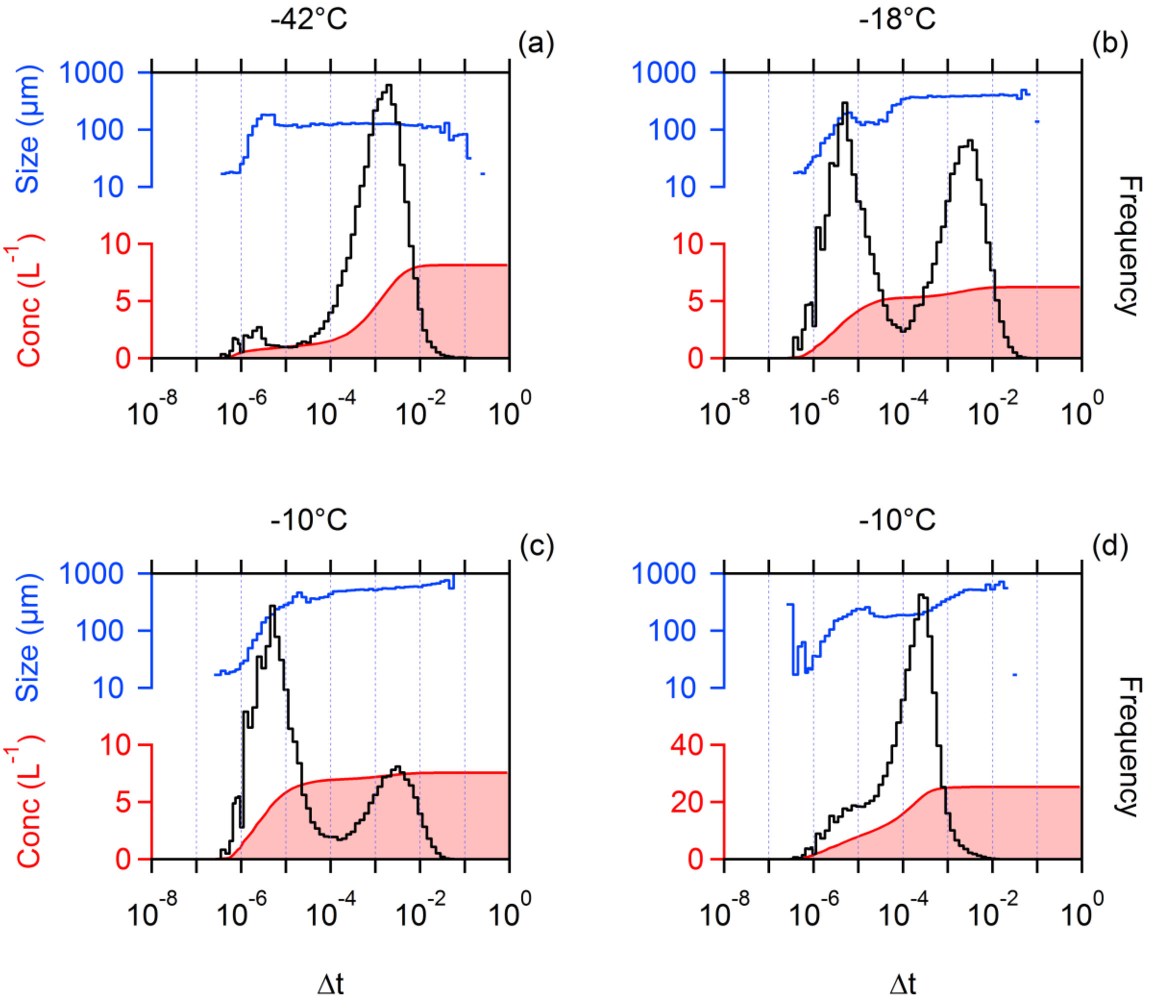

Figure 10: Particle inter-arrival time histograms (black, right axis) for the CIP-15 at -42°C, -18°C and from within and outside the NCFR regions at -10°C (a-d) respectively. Also shown are the mean area equivalent diameter (blue) and the cumulative distribution function (CDF) of the number concentration (red).

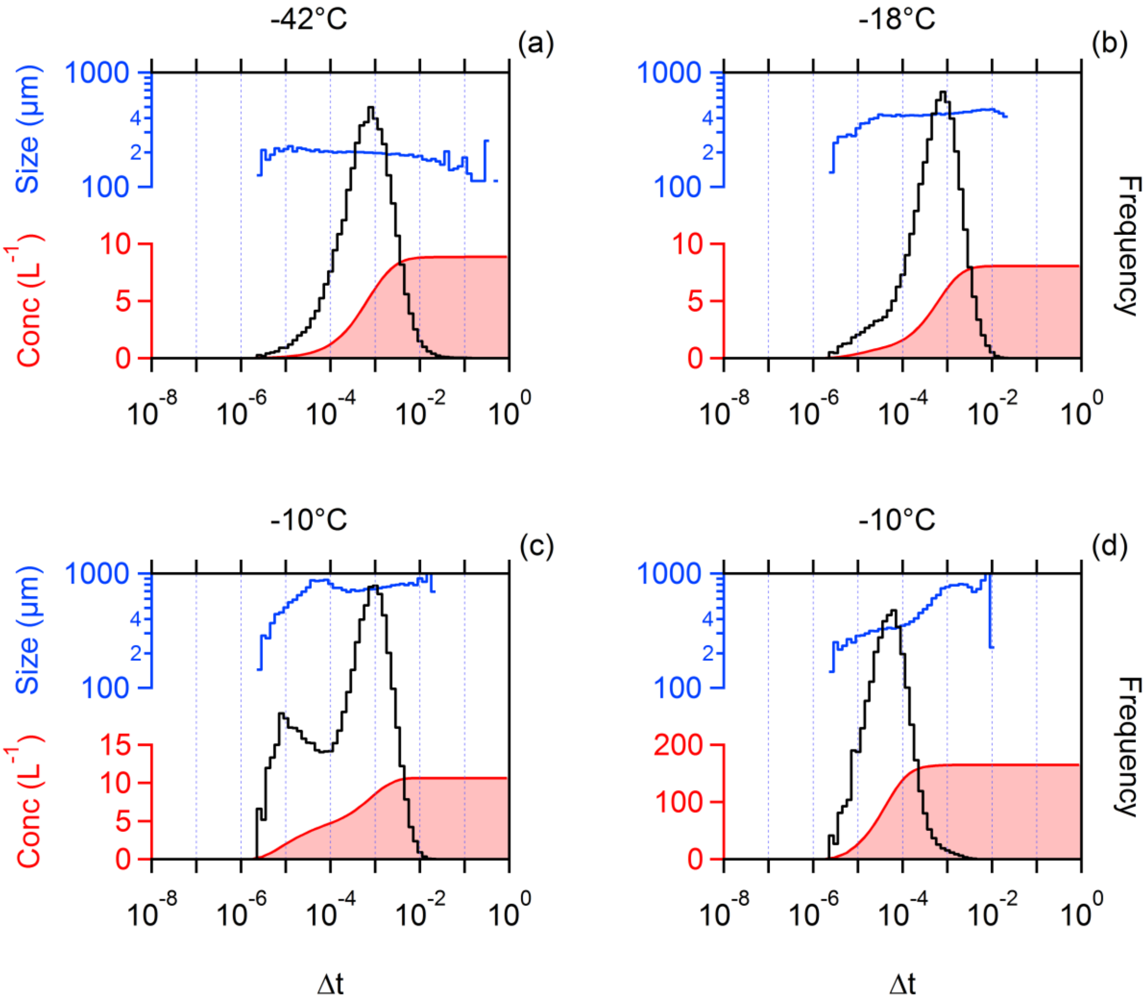

Figure 11: Particle inter-arrival time histograms (black, right axis) for the CIP-100 at -42°C, -18°C and from within and outside the NCFR regions at -10°C (a-d) respectively. Also shown are the mean area equivalent diameter (blue) and the cumulative distribution function (CDF) of the number concentration (red).

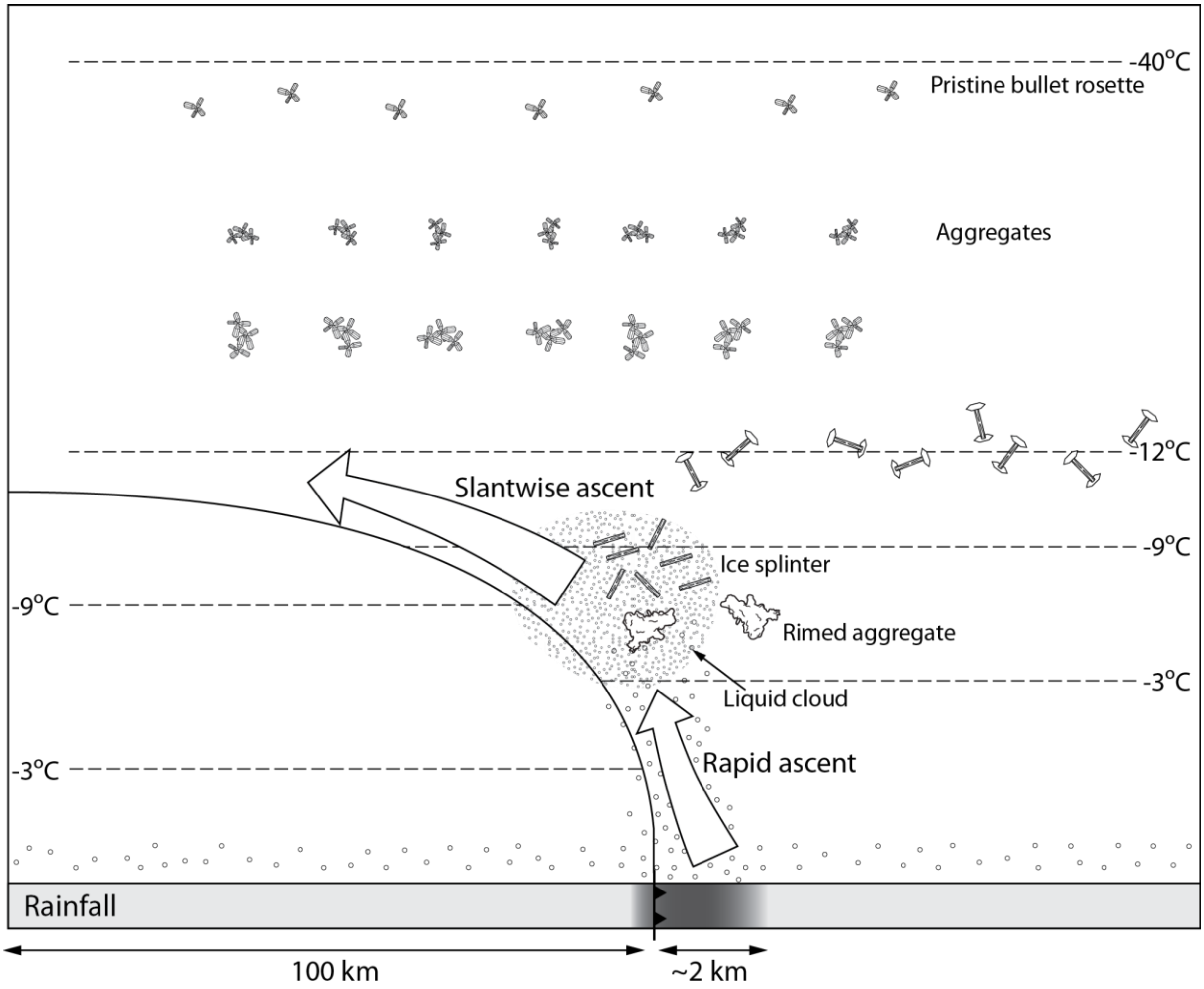

Figure 12: Schematic of microphysical processes controlling ice number concentration and precipitation formation in a Narrow Cold Frontal Rainband.